Method for increasing the core count and area of high density optical fiber bundles

Tarun M. Sanders, Christopher Lamb, Gino Putrino, and Adrian Keating

***Abstract*— Current manufacturing methods limit the increase in both core count and the area for optical fiber bundles. Here a method for increasing the core count and hence the available image area of high density optical fiber bundles, through fusing multiple smaller sized sub-bundles is proposed and experimentally investigated. The key issue being investigated is whether it is possible to eliminate or reduce the dead-space between cylindrical sub-bundles, where no cores are present to spatially sample an image. Small sample lengths of fused optical fiber bundles are fabricated and characterized using an optical and scanning electron microscope to assess the reduction in dead-space and the optical losses near the interfaces. We demonstrate a 30% decrease in the dead-space area through fusing three equally sized sub-bundles in a triangular arrangement, while still retaining the light-guiding ability of more than 70% of the cores which transported into this region. We also assessed the optical losses for cores near the fused interfaces, at different wavelengths in the visible spectrum. A model of the propagation modes supported by the cores is explored which attributes these losses to the increasing eccentricity of cores near the fused interfaces.**

***Index Terms*— Multicore fiber, fiber fabrication and design, optical fiber imaging, linearly polarized modes**

I. Introduction

WHILE the use of high density coherent optical fiber bundles (fiber bundles) have been prominent in the medical and bio-medical fields [1, 2], they have also been utilized in a wide-range of other industrial applications. For instance, fiber bundles have been used for the inspection of defects on surfaces [3], high-resolution Raman imaging [4], and the spatial monitoring of the concentration of various analytes in solution through fluorescence [5, 6]. In many of these industrial applications where restriction in space is not a major limitation, larger sized fiber bundles with a greater field-of-view and high resolution are desirable, for example the imaging in large pipelines for defects.

At present, Schott North America (Schott) manufactures the largest fiber bundles, with their wound image bundle capable of imaging across an available area of up to 38×38 mm^2 and with a core count in the order of millions. However, these fiber bundles are far from ideal for many applications where higher resolution is required, as the resolution available is only 45 lp/mm using diffuse white light illumination. These fiber bundles also have a large individual core diameter of ~10 μm, and also have a low packing density with multiple square 6×6 core sub-bundles making up the entire fiber bundle through a laminating operation [7]. Currently, the largest *high density* fiber bundle is manufactured by Fujikura Ltd, having 100,000 cores confined within an area of 1.54 mm^2 (Fujikura FIGH-100-1500N). However, larger bundles with this high packing density have not yet been manufactured, due to the difficulty of working with the extremely large initial glass array preforms, as well as the low yield and the high costs involved with current manufacturing methods.

In this work, we develop a new alternative method for increasing the core count and available image area for optical fiber bundles through fusing multiple smaller sized sub-bundles, each having a large number of small diameter cores. The lack of research in this area indicates there are considerable barriers to overcome in order to achieve very large area imaging fiber bundles with high density. The key barrier we have identified and investigated in this work is how to use this fusing process to reduce the dead-space area (illustrated in Fig. 1) between cylindrical sub-bundles at the distal (object) end, where no cores are present. A similar fusing approach has been investigated for astronomical applications, however only large single core fibers were fused for purposes of their application [8]. In our work, core distortion in the fused region when fusing multiple existing multicore fiber bundles consisting of thousands of micrometer diameter cores is identified to be an issue, which has not previously been addressed.

Using the developed method, we demonstrate that the dead-space at the fused (distal) end can be reduced by 30%, while still retaining the light-guiding ability of the new cores which now occupy the dead-space. Light was transmitted through the short fused length and the relative losses estimated through the fused set of fiber bundles at various wavelengths in the visible spectrum; blue at 475 nm, green at 560 nm, and red at 640 nm. A model of the propagation modes supported in elliptical fibers as a function of core eccentricity was developed based on the work of Ivan and Ramon [9], which provided insight into the loss mechanisms for the distorted cores in the fused region. This work is primarily focused on understanding the reduction in dead-space at the distal end and the quality of cores in the fused region for the fused set of fiber bundles.

Manuscript received October 1, 2019; revised January 15, 2020.

T. M. Sanders, C. Lamb and A. Keating are with the Department of Mechanical Engineering, The University of Western Australia, Crawley, WA 6009, Australia. (*Corresponding author:* T. M. Sanders, e-mail: tarun.sanders@research.uwa.edu.au)

G. Putrino is with the Department of Electrical, Electronic and Computer Engineering, The University of Western Australia, Crawley, WA 6009, Australia.

II. Fabrication Method

The fabrication method developed in this work is similar to the approach used for fabricating hexabundles for astronomical imaging applications [8], as well as fiber couplers [10], and combiners [11]. In this study, the fusing of the fiber bundles was achieved through the use of a hydrogen flame in air to reach the high temperatures required for processing silica as demonstrated in our previous study [12]. Three small 5 cm length samples of FIGH-06-400N Fujikura fiber bundles were fused for the tests presented here. The short lengths allowed the dead-space region and the fused interfaces to be easily inspected under an optical and scanning electron microscope, while keeping the fabrication costs manageable due to the consumption of the high density fiber bundles during process development.

The individual Fujikura fiber bundles used in this study consisted of 6,000 cores with an average diameter of 3 μm, a pitch of ~4.5 μm [13], and a 15 μm thick surrounding protective silica jacket. Prior to fusing, the silica jacket around each fiber bundle was etched in 10% hydrofluoric acid, and the diameters measured to ensure that only a thickness of 1 μm ±0.5 μm was retained. Once etched the total diameter of the fiber bundle was measured to be approximately 367 μm. The diameters were measured using a dual axis optical gauge from Zhengzhou Mercury-tech Co. Ltd. (LDM2025) with custom made v-groove supports [12]**.** The removal of the silica jacket ensured that the maximum number of cores could fill the dead-space, however the small amount remaining provided isolation to protect the cores at the interfaces during fusing. Three etched fiber bundles were then inserted in a fused quartz capillary tube from VitroCom with an inner diameter of 0.8 mm and wall thickness of 0.1 mm as illustrated in Fig. 1. Through the application of heat, the capillary tube collapses due to surface tension [14] and pushes the heat softened silica fiber bundles together to drive the transport of cores into the dead-space region.

An automated system was developed in this work to achieve high controllability of fusing conditions, consisting of various motorized stages; to control temperature through distance of the hydrogen flame, for rotation of the fibers in the flame at 50 °/s, for brushing the flame back-and-forth at high velocities of 80 mm/s to uniformly fuse over a 1.5 cm length, and for the application of tension to the fibers and capillary to prevent sag due to gravity. The temperature profile with distance from the hydrogen flame was determined through prior measurement using a K-type thermocouple for temperatures up to 1000 °C and estimated for higher temperatures through the melting of various materials including stainless steel (grade 316) at ~1400 °C and fused quartz (type I) at ~1700 °C. The temperature during fabrication was controlled by accurate adjustment of the flame distance to the outer capillary tube. Consistency between fuse runs was achieved by controlling gas flow to the flame and ensuring an in-situ known thermocouple temperature of 950 °C (±50 °C) was obtained at a distance of 3 cm. The fuse length of 1.5 cm was chosen as it provided a sufficient length for subsequent polishing and fuse inspection. This length can be varied through changing the span over which the flame traverses using the linear stage. In practice, when requiring image transmission through fiber bundles across longer distances (meters), the fused length can remain short to minimize losses, but needs to reduce or eliminate the dead-space at the distal end to ensure complete object coverage. The proximal (detector) end does not need to be fused, but image reconstruction requires mapping of cores between the distal and proximal ends using software.

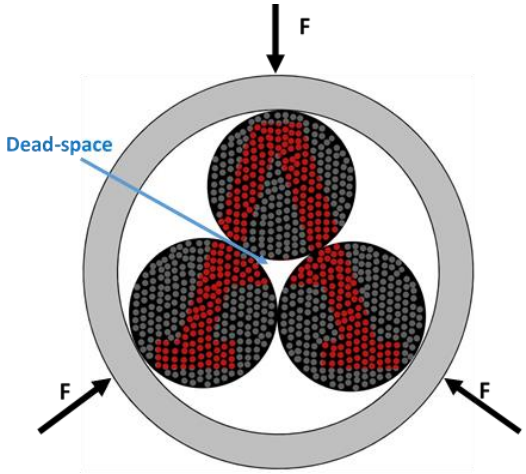

Fig. 1 Illustration of the concept of the dead-space between high density optical fiber sub-bundles, where no cores are present to transmit an image. During fusing the outer capillary tube collapses and applies forces on the internal softened sub-bundles to support mass transport into the dead-space.

III. Characterization of the Dead-space

A. Fuse durations

In Fig. 2, optical microscope images of two fused fiber bundles fabricated through fusing at an estimated temperature of approximately 1600 °C for different durations are presented. These images were taken from the fused end of the samples after illumination of a 50 μm negative grid pattern through the unfused end of the samples. After a fuse duration of only 30 s, Fig. 2(a) indicates that the bundles are only lightly fused at the interfaces. However, fusing for 60 s at these high temperatures was sufficient to reduce the dead-space area between the sub-bundles from an unfused (ideal) area of 5430 μm^2 to a fused area of 3866 μm^2.

The residual dead-space area for the fused fiber bundle in Fig. 2(b) corresponds to ~192 lost cores, or 1.1% based on 18,000 cores in all three fiber bundles. This is almost a 30% improvement from the initial configuration with a dead-space area corresponding to ~270 lost cores. This analysis is based on the fact that a circular area of ~141 μm^2 can contain 7 cores from the FIGH-06-400N Fujikura bundle, with the cores being hexagonally arranged. While effectively 78 cores were recovered in the dead-space after fusing which could transmit image data, these images *a priori* indicate a trade-off with the optical losses near the fused interfaces in the fused region.

B. Image transmission through cores in dead-space

As only one end is fused using this method, in practice the image will be transmitted from the fused (distal) end to the unfused (proximal) end. The optical microscope images

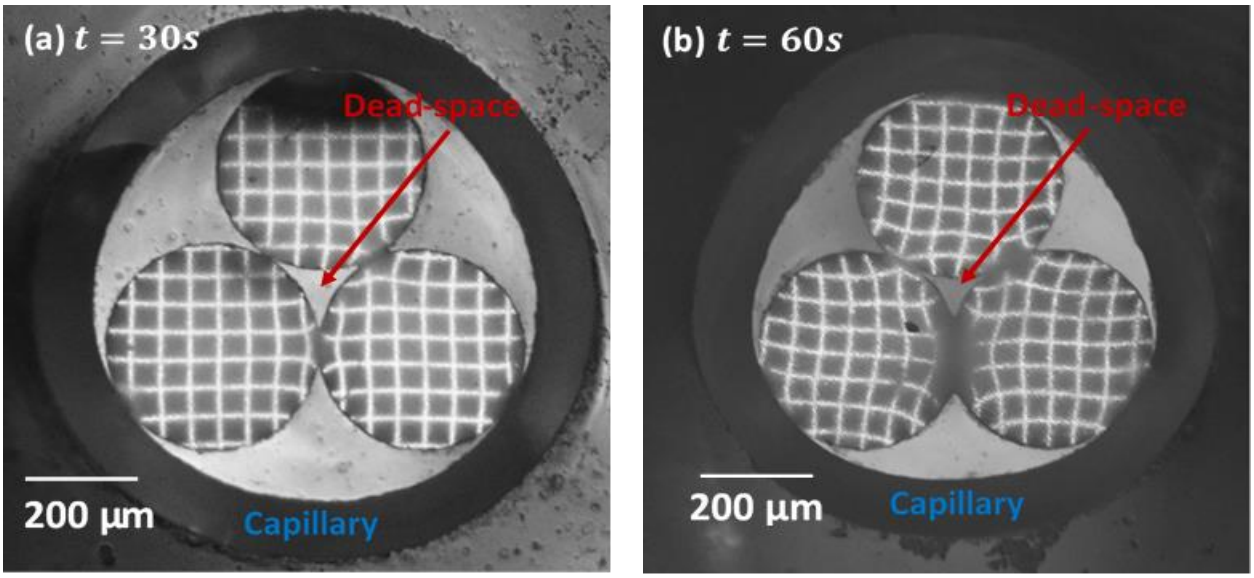

Fig. 2. Optical microscope images of fused optical fiber bundles experiencing an estimated temperature of around1600 ℃ for (a) 30 s and (b) 60 s duration. The top part of the bundle in (a) is black due to cracks and breakage during handling and polishing post fusing.

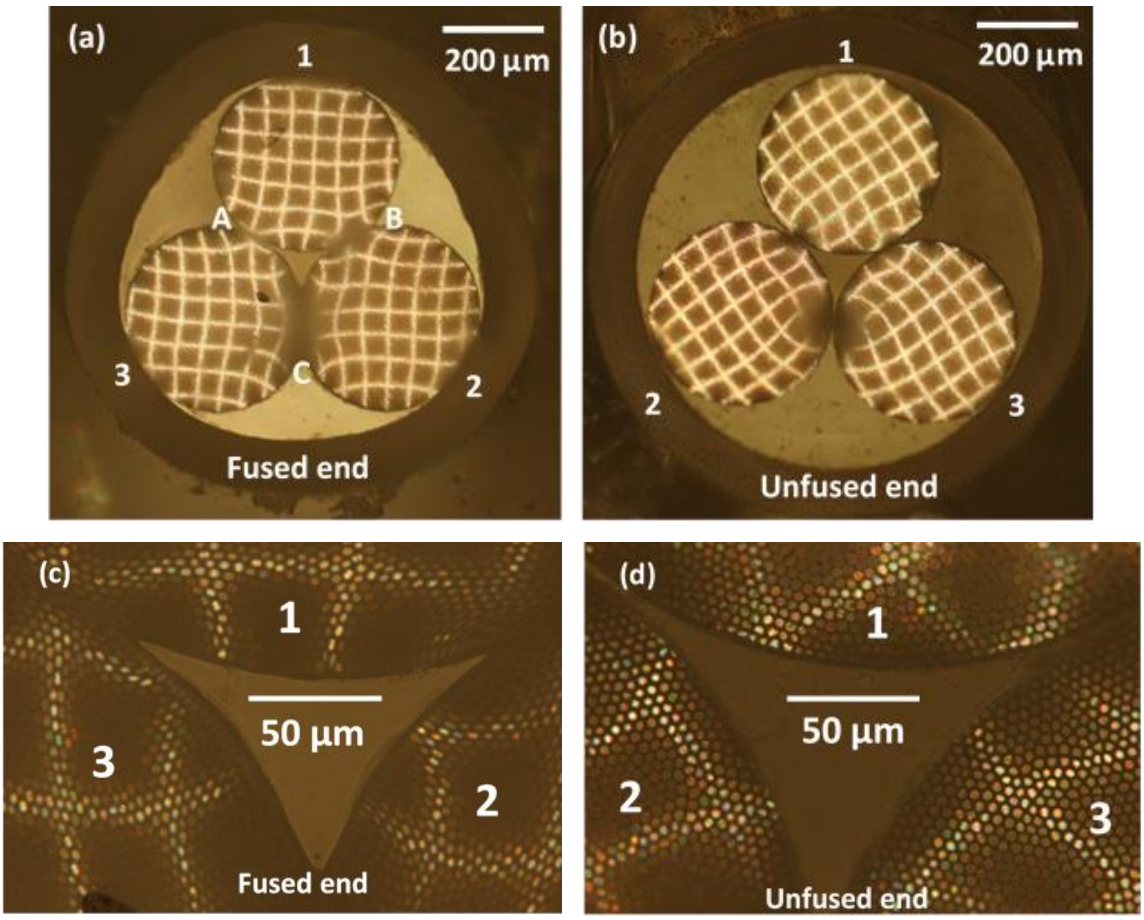

Fig. 3. Optical microscope images of fused fiber bundle with 30% reduced dead-space. In these images a 50 µm negative grid pattern was transmitted. Images are taken at 10x magnification of both the (a) fused end and the (b) unfused end of the fiber bundle, as well as images at 50x magnification of the dead-space for (c) the fused end and the corresponding (d) unfused end.

presented in Fig. 3 depict both the fused and unfused ends of the fused bundle shown in Fig. 2(b). The image of the 50 µm grid pattern was visible through this fused fiber bundle where the distortion of the grid lines is caused by the mass transport of the cores during fusing. However, this distortion can be corrected by mapping the core displacements at the fused end to those cores at the unfused end and using software to reconstruct the original image. The development of a process

for correcting this image distortion is beyond the scope of this study, as our primary aim was to evaluate the reduction in dead-space and quality of cores through the fusing approach. It is important to observe that the cores on the perimeter of the reduced dead-space in Fig. 3(c) preserved their ability to guide an image. This can also be seen in Fig. 3(d), where the image was transmitted in reverse from the fused to the unfused end, where the edges associated with the dead-space display the guided image of the grid-pattern. The significance of this result is that it is possible to recover some of the image within the dead-space of an unfused fiber bundle (see Fig. 1) through the fusing process.

In Fig. 4(a), through backside illumination of all cores from the fused end, we demonstrate that the majority of cores corresponding to the dead-space region on the unfused end of the sample, maintained their light-guiding ability. This is quantified in Fig. 4(b), where the normalized light intensity of the cores along the indicated curve in Fig. 4(a) is profiled from the optical microscope image. The image normalization was performed using the ImageJ software by converting the microscope image into a grey-scale image and normalizing all intensities by the max core intensity found within a selected rectangular section containing a large number of illuminated cores. Around 70% of cores along the profiled curve have an intensity value of between 60 - 90% of the maximum measured intensity with a periodicity between 4 to 5 μm as expected. However, towards the region associated with the fused interfaces on the unfused side of the bundle we see the peak intensities drop below 10% (see Fig. 4(a)-(b)), due to optical losses caused by leaky radiation modes in the fused region. Since, scattering losses are strongly dependent on the core-cladding index difference, which is unchanged by the fusing process other than to reduce it through inter-diffusion, as well as side wall roughness [15], which away from the fused interface is also unchanged, we cannot attribute the loss to scattering. This result suggests a better understanding of the losses near the fused interfaces labelled 'A-C' in Fig. 3(a) is required, which is subsequently discussed.

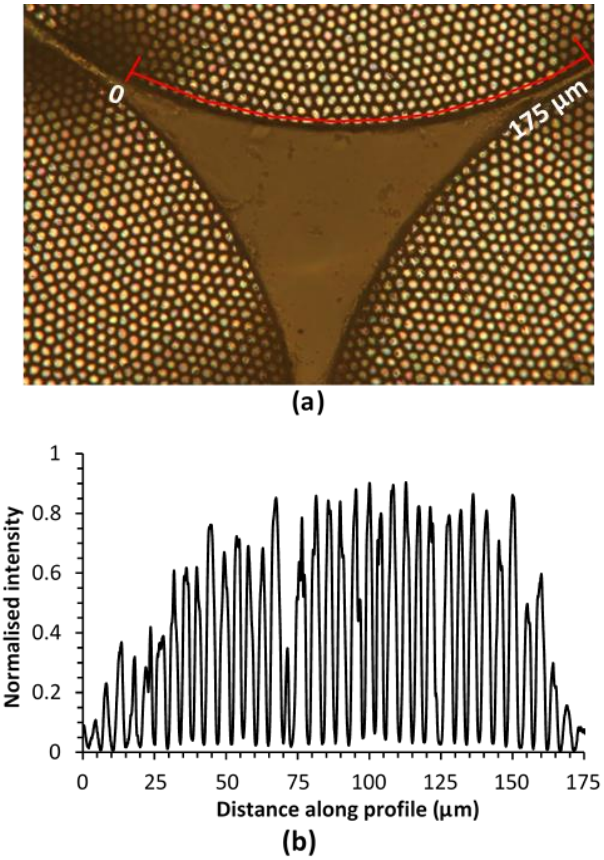

Fig. 4. (a) Optical microscope image with backside illumination of fused fiber bundle with 30% reduced dead-space and (b) the intensity as the normalized grey-value along the profile length indicated in previous image.

IV. Characterization of Fused Interfaces

A. Light intensity at interfaces

The losses near the interfaces were assessed by transmitting light through the fused bundle using a single Tricolor LED at blue, green and red wavelengths in the visible spectrum, as illustrated in Fig. 5. By comparing the wavelength dependence of the loss of each core at these three distinct wavelengths using an incoherent LED source, we were able to able to get a strong indication of the effect of the change of the waveguide parameter (V-number) for the fiber bundles. Electrical switching between the LEDs allowed measurement over a very short time period with minimal movement of the fiber bundle. A broadband source such as an incandescent lamp was not used as it would require several narrow band filters to be mechanically inserted into the optical path which could perturb the measurement and also makes it difficult to characterize our small samples using an optical microscope. Our intent here is not to measure the optical loss in every sub-bundle, but only to correlate the losses with core distortion near the interfaces. Fujikura indicates the optical attenuation ranges from 0.9 dB/m ($\lambda = 400$ nm) to 0.15 dB/m ($\lambda = 650$ nm) for FIGH series fiber bundles [16], and hence propagation loss is not the dominant loss mechanism given the exceedingly short (1.5 cm) fused length. We therefore believe the losses near the interfaces are primarily due to leaky propagation modes [17] well below the cut-off frequency for the distorted cores in the fused region.

The interface labelled 'A' from Fig. 3(a) is studied as it exhibits the least core losses and reduces the complexity of the pursuing analysis, where we correlate these losses to the change in core shape across the interface. The normalized light intensities of cores across this interface were profiled along the lines indicated in Fig. 5 from the corresponding optical microscope images. The corresponding grey-scale images were normalized by the maximum intensity in a selected rectangular region containing many illuminated cores using the ImageJ software, in order to assess the relative drop in intensity across the interfaces for the different wavelengths. It can be observed in the graphs in Fig. 5(a)-(c) that the peaks, which correspond to the cores profiled along the line, drop in intensity towards the interface and the separation between neighboring cores reduces from ~4.5 μm until they are no longer isolated from one another, indicated by the overlapping intensity peaks near the interface.

The losses across the interface appear to be wavelength dependent. In Fig. 5, significant optical losses appear to occur for all wavelengths within 12 μm about interface 'A'. For the

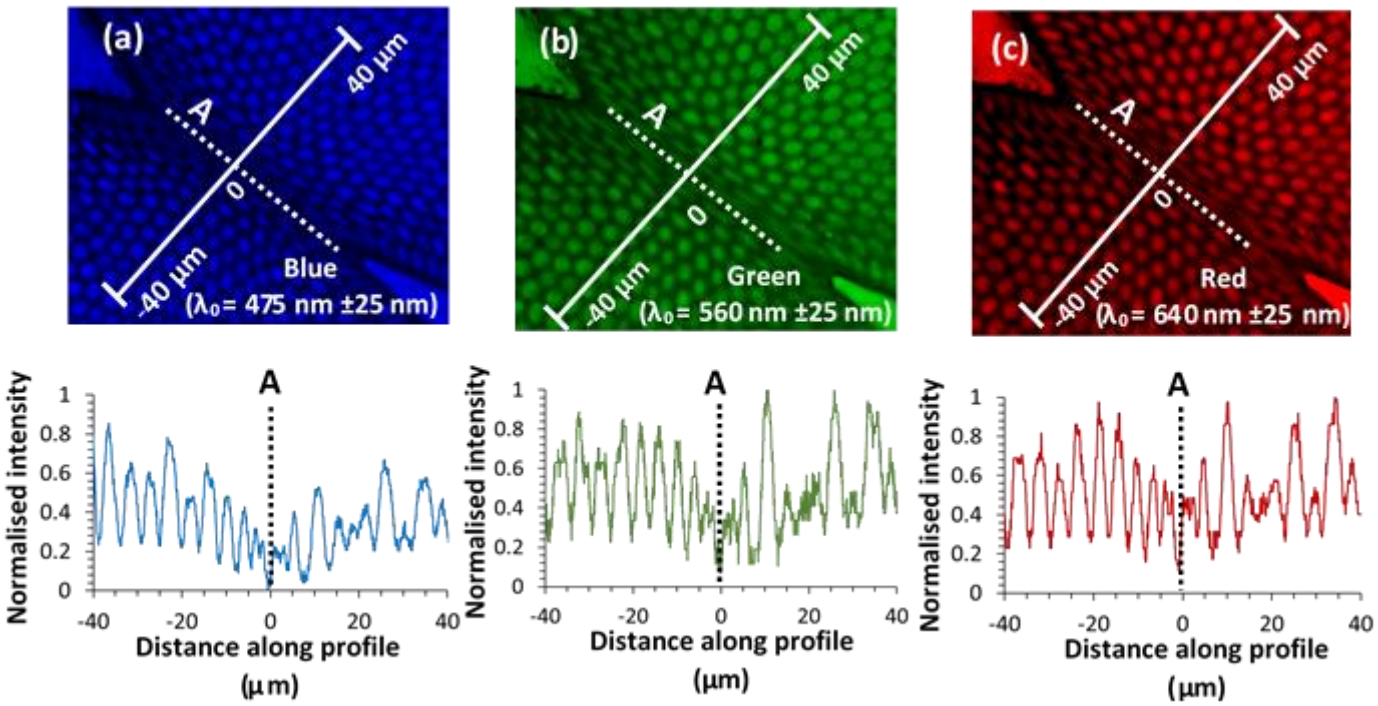

Fig. 5. Fused interface 'A' with plotted intensity values along indicated profile length for backside illumination with (a) blue light with wavelength 475 nm ±25 nm, (b) green light with wavelength 560 nm ±25 nm, and (c) red light with wavelength 640 nm ±25 nm. All images here are enhanced in contrast for presentation.

shorter wavelength in the blue region it is found that within 12 µm about the interface the relative core light intensity dropped 30% (see Fig. 5(a)). Whereas, for the longer wavelengths in the green and red regions it is found that within 12 µm the relative intensity drop was larger than 50% (see Fig. 5(b)-(c)). It is believed that the reason for the reduced light intensity is due to a reduction in the number of propagation modes supported by the highly elliptical cores near the interface at the fused end of the fiber bundle, as depicted by the scanning-electron microscope (SEM) image in Fig. 6(a).

The increasing eccentricity of cores towards the interface is indicated by the decreasing ratio of the minor to major axes (axis ratio) of the fitted core ellipses towards the interface in Fig. 6(b). Through the image processing of an SEM image of an unfused fiber bundle, the mean core axis ratio was determined to be 0.8 with a standard deviation of 0.1 for a sample size of 346 detected cores. This average and uncertainty in axis ratios for unfused fiber bundles is also shown in Fig. 6(b), which indicates that cores further than 12 µm about interface 'A' settle within this uncertainty range. This finding is highly suggestive that the large optical losses observed within 12 µm about the interface is attributed to the increased eccentricity of cores near the interfaces at the fused end. The increased eccentricity of cores is caused by the mass transport during the fusing event. During fusing, the collapse of the external capillary tube exerts a force on the softened internal sub-bundles which pushes them together. This results in the cores near the interface being squeezed closer to each other and elongating as a result of conservation of mass (see Fig. 6(a)) assuming no transport out-of-the-plane.

The number of propagation modes supported by a core depends on the normalized frequency or V-number defined by,

$$V = \frac{2\pi b}{\lambda_0}(n_{core}^2 - n_{cl}^2)^{1/2}. \quad (1)$$

where b is the semi-minor axis length of the core, λ_0 the free space wavelength, and n_{core} and n_{cl} the core and cladding refractive indices respectively. In general, the larger the normalized frequency the greater the number of high order modes which can be supported. Thus, for longer wavelengths and smaller cores, fewer bound modes are supported leading to greater light loss. From (1), it is clear that wavelengths in the blue region have a larger normalized frequency in comparison to the longer wavelengths in the green and red regions of the visible spectrum. Since, the cut-off frequency for modes in elliptical cores is further complicated by the fact that it also depends on the core eccentricity, we proceed to calculate the normalized cut-off frequency for various modes as a function of core eccentricity. This way the potential modes supported by cores across the interface can be studied.

B. Mode filtering at the interfaces

The modes in elliptical waveguides were originally analyzed in 1962 by Yeh [18]. The calculation of modes in elliptical waveguides are considerably more complicated than their circular counterparts, as they exhibit a property known as birefringence [9, 19], where the modes degenerate into even and odd modes with slightly differing propagation constants, β. This is due to different lengths associated with the semi-minor and semi-major axes of elliptical cores. The analysis of modes in these waveguides were simplified by using the weakly

This article has been accepted for publication in a future issue of this journal, but has not been fully edited. Content may change prior to final publication. Citation information: DOI 10.1109/JSTQE.2020.2984562, IEEE Journal of Selected Topics in Quantum Electronics

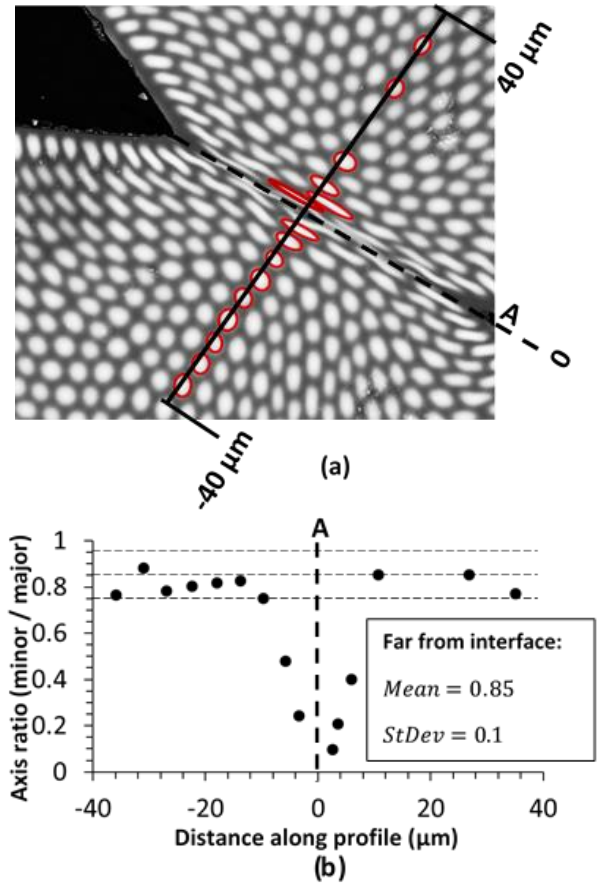

Fig. 6. (a) Scanning-electron microscope image of interface 'A' of the fused-bundle showing the fitted ellipses along the profile length indicated and (b) a plot of the axis ratio of the fitted cores along the profile length.

guiding approximation [20-22], where the modal field can be considered to be nearly transverse and linearly polarized (LP) when the refractive index contrast between the core and cladding is small [17]. In the weakly guiding analysis, the transverse modal fields for elliptical waveguides are solved from the scalar wave equation in an elliptical coordinate system, (ξ, η), where the solutions are known to be the so-called Mathieu functions [20, 21]. The modes are then determined from the characteristic equations, which are derived through application of the boundary conditions requiring continuity of the modal field and its normal derivative at the core-cladding interface, $\xi = \xi_0$. In this work, the normalized cut-off frequencies for selected even and odd LP modes, designated as the $\mathrm{LP}_{\mathrm{mn}}^{E}$ and $\mathrm{LP}_{\mathrm{mn}}^{O}$ modes respectively, were computed using the method developed by Ivan and Ramon [9].

In Fig. 7(a) the normalized cut-off frequencies for the LP_{11}^{E}, LP_{11}^{O}, LP_{02}^{E}, LP_{12}^{E}, LP_{12}^{O}, LP_{22}^{E}, LP_{22}^{O}, LP_{03}^{O}, LP_{41}^{E} and LP_{41}^{O} modes were computed for an axis ratio in the range between 0.1 to 1, to aid discussion of the optical losses at the interfaces for our fabricated fused fiber bundles. It is to be noted that the normalized cut-off frequencies for the LP_{x1} modes monotonically increase with x for both the even and odd modes, however all the modes in the range $1 < x < 4$ are not displayed in Fig. 7(a) for convenience of presentation. The few points computed by Ivan and Ramon [9], with axis ratios in the range between 0.5 to 1, lie on the curves produced in Fig. 7(a). Furthermore, the curves for the LP_{11}^{E}, LP_{11}^{O}, and LP_{02}^{E} modes in

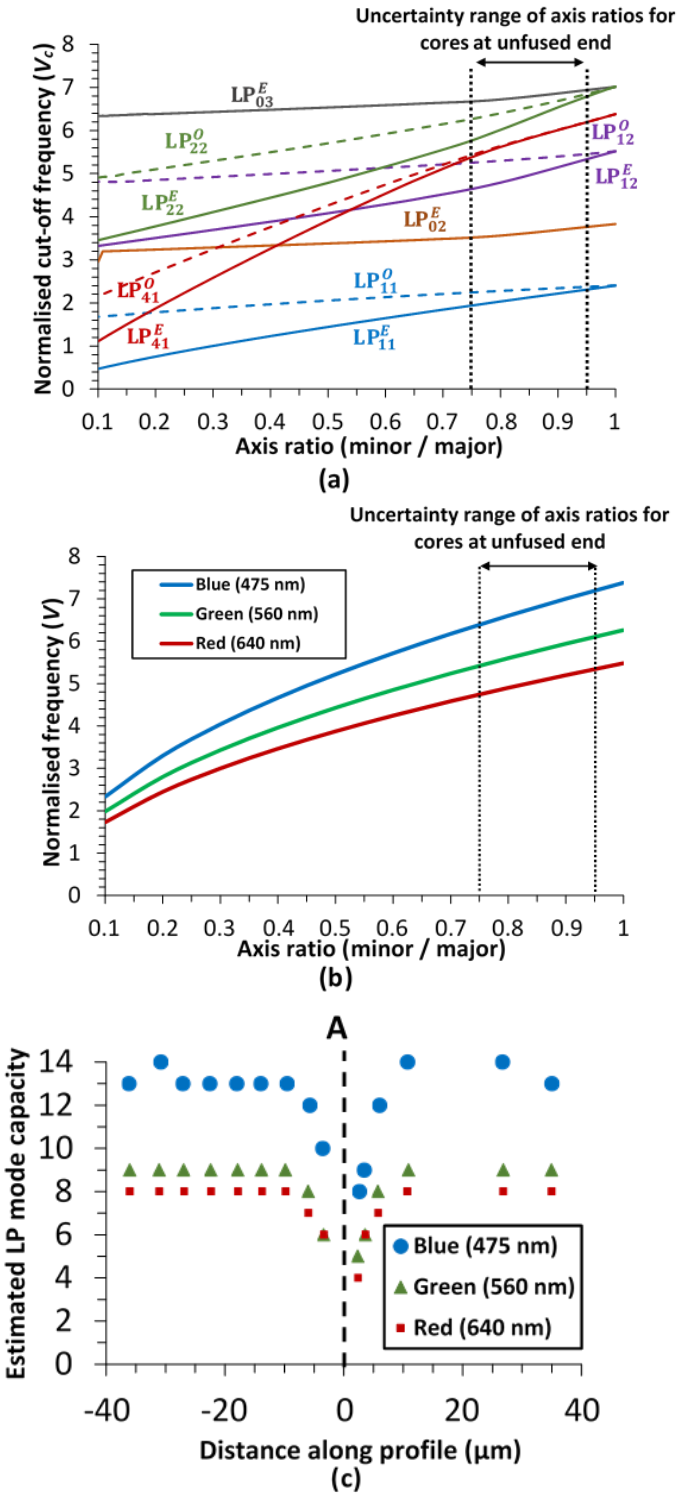

Fig. 7. (a) Normalized cut-off frequencies of various LP modes and (b) the normalized frequencies as a function of axis ratios for the blue, green and red wavelengths studied. (c) Estimated LP mode capacity of cores along the profile across interface 'A'.

Fig. 7(a) lie in a similar range as that computed in other studies using finite-element methods [23]. For all the curves, the normalized cut-off frequency for an axis ratio approaching 1 are extremely close to that computed for circular waveguides [24], which provides confidence for all the computations performed in this work.

For the fiber bundles used in this work, the normalized frequency for the same range of axis ratios were estimated for the blue, green and red wavelengths as depicted in Fig. 7(b). This estimation is based on the mean area of all cores being 6.4 μm^2 with a standard deviation of 1.1 μm^2, which again was determined from the image processing of an SEM image of an unfused fiber bundle across a sample size of 346 detected cores. Assuming an elliptical shape for a core, using this mean area, the semi-minor axis length, b, can be determined and therefore using (1) the normalized frequency calculated for any axis ratio, knowing that the core and cladding refractive indices of these bundles are 1.5 and 1.446 respectively [13]. It is observed in Fig. 7(b) that for all the wavelengths the normalized frequency drops rapidly for cores with decreasing axis ratio, as would be expected due to the decreasing semi-minor axis length. The normalized frequency associated with a core at a specific wavelength in Fig. 7(b) must be greater than the cut-off frequency for a mode in Fig. 7(a), in order for it to be supported.

Since, for Fig. 5 light is launched from the unfused end to the fused end of the fiber bundle, only those modes which are supported by the nearly circular cores at the unfused end can propagate. While intermodal coupling between higher order modes is possible, it can be considered negligible as it requires the propagation constant, β, between modes to be similar in value and generally requires longer distances for any power exchange between modes to occur [25]. In Fig. 7(a)-(b), the uncertainty range of the axis ratios of the nearly circular cores at the unfused end are indicated. For the blue wavelength for an axis ratio above 0.85, all the LP modes displayed in Fig. 7(a) are potentially supported. However, at this wavelength for an axis ratio below 0.85, the LP_{03}^{E} cannot be supported, thus there is some uncertainty whether this mode can be supported at all throughout the length of the fused fiber bundle (see Fig. 7(a)-(b)). Likewise, for the green wavelength, the LP_{03}^{E}, LP_{22}^{E}, LP_{22}^{O}, LP_{41}^{E} and the LP_{41}^{O} cannot be supported by the nearly circular cores (see Fig. 7(a)-(b)). In addition to the previous, the LP_{12}^{O} mode cannot be supported for the red wavelength (see Fig. 7(a)-(b)).

As light propagates to the fused end of the fiber bundle, due to increased eccentricity of the cores near the interface (see Fig. 6(b)) and consequently a decrease in the normalized frequency at the different wavelengths (see Fig. 7(b)), a greater number of higher order modes are filtered by these cores. For an axis ratio as low as 0.1, the LP_{03}^{E}, LP_{12}^{E}, LP_{12}^{O}, LP_{22}^{E}, LP_{22}^{O} and the LP_{02}^{E} modes are no longer supported under the blue wavelength. Likewise, under the green wavelength the LP_{02}^{E}, LP_{12}^{E}, LP_{12}^{O} and the LP_{31}^{O} (not shown in Fig. 7(a)) modes cannot be supported, in addition to the ones that cannot normally propagate by the nearly circular cores. For the red wavelength, in addition to the previous the LP_{21}^{O} (not shown in Fig. 7(a)) mode cannot be supported for this low axis ratio.

Based on the axis ratios for the cores across interface 'A' along the profile in Fig. 6, the estimated number of bound LP modes supported by each of these cores is determined and displayed in Fig. 7(c). The significant drop in LP mode capacity for cores within 12 μm about the interface (see Fig. 7(c)) explains the significant optical losses observed in Fig. 5. Since for the longer green and red wavelengths there are less modes supported by the nearly circular cores far from the interface, the high degree of mode filtering by the elongated cores should have a greater impact in the relative drop in light intensity across the interface (see Fig. 7(c)). This is in fact supported experimentally, where it was observed that there was a greater relative drop within 12 μm about the interface for the green and red wavelengths in comparison to the blue wavelength (see Fig. 5).

This study of the modes supported as a function of core eccentricity, provides insight into the loss mechanisms for cores across the interface for fused fiber bundles. For axis ratios below 0.5 the number of higher-order modes supported by the cores at the three wavelengths studied appears to drop rapidly (see Fig. 6 and Fig. 7), and results in significant optical losses at the interfaces in the visible spectrum. Thus, the fusing method needs to be optimized in order to reduce the elongation of cores and minimize losses at the interface, while recovering a greater number of cores in the dead-space. Therefore, potential methods to further reduce the dead-space and losses at the interfaces are subsequently discussed.

V. Future Pathways

While fusing for longer durations or at higher temperatures will enable us to reduce the dead-space area further, this would result in greater optical losses at the interfaces due to increased core distortion. A potential solution to this problem is to reduce the initial dead-space area by inserting an even smaller sub-bundle into the gap as illustrated in Fig. 8. From purely geometric arguments, the area of a single gap after insertion of smaller fiber bundle as depicted in Fig. 8, would be 82% smaller than the total dead-space area without insertion. A small dead-space would only need a short fusing duration leading to less overall distortion. This improvement is reserved for future work, as significant process development is required for the selection, preparation, handling and characterization of the mixed-size fiber bundles.

Alternatively, we could reshape the distal (object) end of the fiber bundles into a hexagonal shape and mate multiple fiber bundles to form a larger hexagonal array [26]. However, this solution requires high precision side-polishing [26] due to the small 3 μm diameter core sizes within the fiber bundles. Furthermore, this process would result in a significant number of unusable fiber cores at the proximal (imaging) end due the removal of these cores at the distal end.

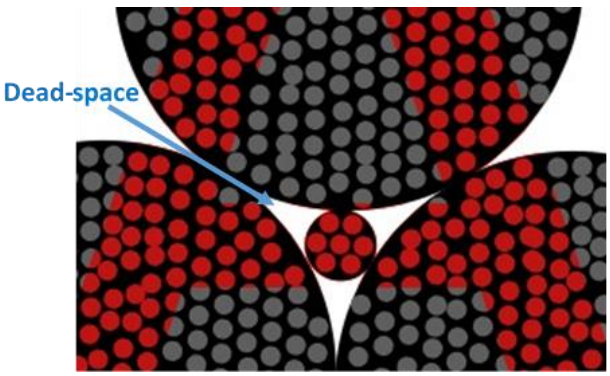

Fig. 8. Illustration of the modification of the dead-space area through the insertion of a smaller fiber sub-bundle between the three large sub-bundles.

VI. Conclusion

In this work we presented a promising alternative fabrication approach for increasing the core count and available image area through a fusing process. We demonstrate a reduction of the dead-space area by 30% through a short length fusing process, while still retaining the light-guiding ability of more than 70% of cores which transported into the dead-space. Optical losses are found to be associated with the cores in the fused region and are attributed to the increased core eccentricity, where cores reached axis ratios below 0.1. This was supported by a model showing that a greater number of higher order modes were filtered by the cores with increased eccentricity near the interfaces on the fused end. This study presents the first step towards realizing a fully developed and pragmatic alternative approach for fabricating large high density fiber bundles, potentially overcoming the difficulty faced by current manufacturing methods to further increase both the core count and the available image area.

Acknowledgment

We would like to thank Mr. Yoshida and Mr. Suzaki from Fujikura Ltd. Japan for support with providing the fiber bundles associated with this work. Fiber etching was performed at the Western Australian Node of the Australian National Fabrication Facility, a company established under the National Collaborative Research Infrastructure Strategy to provide nano- and micro-fabrication facilities for Australia's researchers.

References

[1] V. Dubaj, A. Mazzolini, A. Wood, and M. Harris, "Optic fibre bundle contact imaging probe employing a laser scanning confocal microscope," *J. Microsc.*, vol. 207, no. 2, pp. 108-117, 2002.

[2] M. Hughes, T. P. Chang, and G.-Z. Yang, "Fiber bundle endocytoscopy," *Biomed. Opt. Express*, vol. 4, no. 12, pp. 2781-2794, 2013.

[3] L. Bin, W. Quan, T. Jun, D. A. Dwayne, and Z. Dongsheng, "Inspection of the interior surface of cylindrical vessels using optic fiber shearography," *Meas. Sci. Technol.*, vol. 28, no. 9, p. 095202, 2017.

[4] L. V. Doronina-Amitonova, I. y. V. Fedotov, A. B. Fedotov, and A. M. Zheltikov, "High-resolution wide-field Raman imaging through a fiber bundle," *Appl. Phys. Lett.*, vol. 102, no. 16, p. 161113, 2013.

[5] P. Pantano and D. R. Walt, "Analytical Applications of Optical Imaging Fibers," *Anal. Chem.*, vol. 67, no. 15, pp. 481A-487A, 1995.

[6] C. Amatore *et al.*, "Remote Fluorescence Imaging of Dynamic Concentration Profiles with Micrometer Resolution Using a Coherent Optical Fiber Bundle," *Anal. Chem.*, vol. 76, no. 24, pp. 7202-7210, 2004.

[7] H. D. Ford and R. P. Tatam, "Characterization of optical fiber imaging bundles for swept-source optical coherence tomography," *Appl. Opt.*, vol. 50, no. 5, pp. 627-640, 2011.

[8] J. Bland-Hawthorn *et al.*, "Hexabundles: imaging fiber arrays for low-light astronomical applications," *Opt. Express*, vol. 19, no. 3, pp. 2649-2661, 2011.

[9] G.-C. Ivan and M. R.-D. Ramon, "Intensity distributions and cutoff frequencies of linearly polarized modes for a step-index elliptical optical fiber," *Opt. Eng.*, vol. 46, no. 4, pp. 1-11, 11, 2007.

[10] T. A. Birks, "Effect of twist in 3 × 3 fused tapered couplers," *Appl. Opt.*, vol. 31, no. 16, pp. 3004-3014, 1992.

[11] A. Kosterin, V. Temyanko, M. Fallahi, and M. Mansuripur, "Tapered fiber bundles for combining high-power diode lasers," *Appl. Opt.*, vol. 43, no. 19, pp. 3893-3900, 2004.

[12] T. M. Sanders, G. Putrino, and A. Keating, "Investigation of a novel method for the fabrication of larger area imaging fibre bundles with greater number of pixels and reduced dead space," in *2018 Conference on Optoelectronic and Microelectronic Materials and Devices (COMMAD)*, 2018, pp. 27-30: IEEE, 2018.

[13] X. Chen, K. L. Reichenbach, and C. Xu, "Experimental and theoretical analysis of core-to-core coupling on fiber bundle imaging," *Opt. Express*, vol. 16, no. 26, pp. 21598-21607, 2008.

[14] J. A. Lewis, "The collapse of a viscous tube," *J. Fluid Mech.*, vol. 81, no. 1, pp. 129-135, 1977.

[15] D. Melati, F. Morichetti, and A. Melloni, "A unified approach for radiative losses and backscattering in optical waveguides," *J. Opt.*, vol. 16, no. 5, p. 055502, 2014.

[16] Q. Lin, "Transmission Characteristics of Fujikura's Image Fibers," Fujikura Ltd, Japan, Tech. Report. No.B-09D2040, 4 Sept. 2009.

[17] A. W. Snyder and W. R. Young, "Modes of optical waveguides," *J. Opt. Soc. Am.*, vol. 68, no. 3, pp. 297-309, 1978.

[18] C. Yeh, "Elliptical Dielectric Waveguides," *J. Appl. Phys.*, vol. 33, no. 11, pp. 3235-3243, 1962.

[19] S. R. Rengarajan, "On higher order mode cutoff frequencies in elliptical step index fibers," *IEEE Trans. Microwave Theory Tech.*, vol. 37, no. 8, pp. 1244-1248, 1989.

[20] J. K. Shaw, W. M. Henry, and W. R. Winfrey, "Weakly guiding analysis of elliptical core step index waveguides based on the characteristic numbers of Mathieu's equation," *J. Lightwave Technol.*, vol. 13, no. 12, pp. 2359-2371, 1995.

[21] C. Yeh, "Modes in weakly guiding elliptical optical fibres," *Opt. Quantum Electron.*, journal article vol. 8, no. 1, pp. 43-47, Jan. 1976.

[22] W. Ye Heng and Z. Xiang, "Elliptical Fourier series expansion method together with cutoff frequencies in elliptical optical waveguides," *J. Lightwave Technol.*, vol. 16, no. 10, pp. 1933-1941, 1998.

[23] H. Soren, "Measured and simulated cutoff wavelengths as a function of core ellipticity for higher order modes in elliptical optical fibers," *Opt. Eng.*, vol. 49, no. 12, pp. 1-7, 7, 2010.

[24] A. W. Snyder and J. Love, *Optical Waveguide Theory*. Springer US, 2012.

[25] S. Shaklan, "Measurement of intermodal coupling in weakly multimode fibre optics," *Electronics Letters*, vol. 26, no. 24, pp. 2022-2024, 1990.

[26] D. Liang, L. Fraser Monteiro, M. Ribau Teixeira, M. L. Fraser Monteiro, and M. Collares-Pereira, "Fiber-optic solar energy transmission and concentration," *Solar Energy Materials and Solar Cells*, vol. 54, no. 1, pp. 323-331, 1998.

Tarun M. Sanders obtained a B.E. degree in electrical and electronic engineering in 2017 from the University of Western Australia (UWA), Perth. He is currently working towards a Ph.D. degree with the department of Mechanical Engineering in UWA. He has previous experience with III-V nitride materials, x-ray photoelectron spectroscopy, numerical modelling as well as optical fiber technology for high quality imaging.

Christopher Lamb obtained a B.Sc. degree in mechanical engineering from UWA in 2018. In 2018 he started working at UWA as a researcher focusing in areas of precision systems and manufacturing. He has built a fleet of FDM 3D printers for UWA and designed and manufactured a polishing system for optical fiber technology.

Gino Putrino is a researcher at UWA. He received the B.Sc. degree in computer science and the B.E. degree in electrical and electronic engineering from UWA in 1999. He received the Ph.D. degree in the School of Electrical, Electronic and Computer Engineering at UWA in 2014. His research interests include combining optics, silicon photonics and MEMS to create novel structures for sensing applications. He is the current Chair of the IEEE West Australian Joint Chapter of the Electron Devices, Solid State Circuits and Photonics Societies.

Adrian J. Keating (IEEE M'90-SM'07) received his B.E. and Ph.D. degrees in electrical and electronic engineering from the University of Melbourne, Australia in 1990 and 1995 respectively. He has worked with NTT in Japan (1996) on high speed communication systems, at UCSB (1998) investigating long wavelength VCSEL, and at Calient Networks (1999). He became Associate Professor in Mechanical Engineering at UWA in 2010 and his current research activities include microelectro-mechanical systems (MEMS), fiber optic system, porous silicon based sensor technologies and energy harvesting systems.